CRYSTAL GROWTH & DESIGN
2009
VOL. 9, NO. 7
3024–3030

Synthesis and Growth Mechanism of One-Dimensional Zn/ZnO Core−Shell Nanostructures in Low-Temperature Hydrothermal Process

Martín Trejo,[†,||] Patricia Santiago,*[,†] Hugo Sobral,[‡] Luis Rendón,[†] and Umapada Pal[§]

Departamento de Materia Condensada, Instituto de Física, Universidad Nacional Autónoma de México, Coyoacan, 04510, A.P. 20-364, 01000 Mexico D.F., Mexico, ESIQIE-Instituto Politécnico Nacional, Zacatenco, Mexico, D.F. 07738, Mexico, Centro de Ciencias Aplicadas y Desarrollo Tecnológico, Universidad Nacional Autónoma de Mexico, Apartado Postal 70-186, Mexico DF. 04510, México, and Instituto de Física, Benemérita Universidad Autónoma de Puebla, Apdo. Postal J-48, Puebla, Pue. 72570, Mexico

Received February 8, 2008; Revised Manuscript Received March 31, 2009

ABSTRACT: Binary metal-semiconductor Zn/ZnO core−shell nanorods have been synthesized through an ethylenediamine-assisted low-temperature hydrothermal process. Well-crystalline wurtzite phase ZnO was epitaxially grown along the [0100] direction, perpendicular to the single-crystalline Zn nanorod cores grown along the [0002] direction. The structure and optical properties of the binary metal-semiconductor nanostructures were studied by SEM, HRTEM, absorption, and emission spectroscopy techniques. The mechanisms for the growth of such binary structures in solution based synthesis are discussed. The growth technique can be extended for the preparation of other hybrid nanostructures.

Introduction

Contemporary technologies have stimulated great interest in searching a new generation of materials that serve as the basis for the development of functional devices. For example, the competition of making the next generation of compact disk (CD) read-heads involved several research groups around the world. The shorter the wavelength of the operating laser, the higher the quantity of information that can be stored by such device. However, the band gaps of most of the conventional semiconductors are not large enough to generate UV light. The ZnO has a broadband gap energy of 3.37 eV at room temperature, which is suitable for short wavelength emissions. Its high exciton binding energy (60 meV) can ensure an efficient excitonic emission at room temperature under low excitation intensity. However, UV stimulated emissions and lasing from bulk ZnO materials were observed only at cryogenic temperatures.[1−3] Recently, very interesting UV emissions in ZnO thin films grown by laser-assisted molecular beam epitaxy (MBE)[4] and other ZnO nanostructures[5] are observed. Observation of room-temperature UV lasing from the ordered ZnO nanocrystals[6] enhanced the prospect for the development of practical blue UV lasers. Varieties of ZnO nanostructures such as nanocombs, nanobelts, nanorods, tretapods, etc., could be prepared by using a vapor−solid technique, whose main advantages are the use of simple synthesis equipment (e.g., tubular furnaces) and moderate temperatures (400−700 °C).[5,7] On the other hand, hydrothermal techniques allow us to prepare ZnO nanostructures at even lower temperatures (<100 °C) using cheaper laboratory equipments.[8] The synthesis conditions used in the latter techniques are compatible with other soft chemistry approaches, such as the sol−gel method.

In this work, we used a low-temperature hydrothermal approach for the preparation of one-dimensional core−shell Zn/ZnO nanostructures. Structural and optical properties of the samples are studied using different characterization techniques, and the mechanisms for their growth are discussed.

Experimental Section

Hydrothermal synthesis of the Zn/ZnO core−shell one-dimensional (1D) structures was studied for Zn^{2+} concentration range of 0.364−0.72 mol/L. In a typical synthesis process, 0.0182 mol of zinc acetate dihydrate (Fluka, grade pH Eur) was added to 25 mL of a 10% (v/v) ethylendiamine (En) aqueous solution (pH 11.93) under stirring. A transparent solution was obtained and the pH of the mixture solution reduced to 9.27. This solution was directly poured into an autoclave of 60 mL capacity, and the closed autoclave was introduced into an oven at 92 °C. Different samples were prepared by varying the thermal treatment time from 8 h to 3 days. Once the thermal treatment was over, the oven was turned off and the temperature was gradually decreased to room temperature using a cooling rate of 1 °C/90 s. For only the samples with thermal treatment longer than 1 day, white precipitates were observed at the bottom of the autoclave container. The precipitate, which was surrounded by a pale-yellow solution, were filtered and washed several times by deionized water and finally dried at room temperature. The 1D nanorod structures were obtained when the cation concentration was higher than 0.637 mol/L. The color of the final reaction solution was yellow when the Zn^{2+} concentrations were slightly lower than this value.

The synthesis of pure ZnO nanorod structures was realized using a technique similar to one described earlier.[8] For obtaining pure ZnO nanostructures, 0.0218 mol of zinc acetate dihydrate was slowly added to 50 mL of a 10% (v/v) En mixture under vigorous stirring. A transparent solution with a pH value of 10.63 was obtained. The pH of this solution was increased to reach about 11.5 by adding few drops of a NaOH (18M) solution. The mixture solution remained transparent and no precipitate formation was observed. This solution was then poured into an autoclave which was put into an oven at 92 °C for 48 h. The oven was cooled to room temperature, and white precipitates were formed at the bottom of the autoclave container. The color of the surrounding solution was also pale yellow. These precipitates were filtered and washed several times by deionized water and dried at room temperature. Obtained samples were annealed in air at 240 °C for 2 h.

The morphology and structural properties of the products were studied by scanning electron microscopy (JEOL 5600 LV-SEM) and transmission electron microscopy (TEM, JEM 2010 FasTem equipped with a Noran EDS spectrometer). For TEM observations, a drop of sample dispersed in ethanol was spread onto a carbon-coated copper grid and dried in a vacuum.

* To whom correspondence should be addressed. E-mail: paty@fisica.unam.mx. Telephone: (525) 55 56225033. Fax: (525) 55 56225011.
[†] Universidad Nacional Autónoma de México.
[‡] Centro de Ciencias Aplicadas y Desarrollo Tecnológico UNAM.
[||] ESIQIE-Instituto Politécnico Nacional.
[§] Benemérita Universidad Autónoma de Puebla.

10.1021/cg8001493 CCC: $40.75
Published on Web 05/12/2009

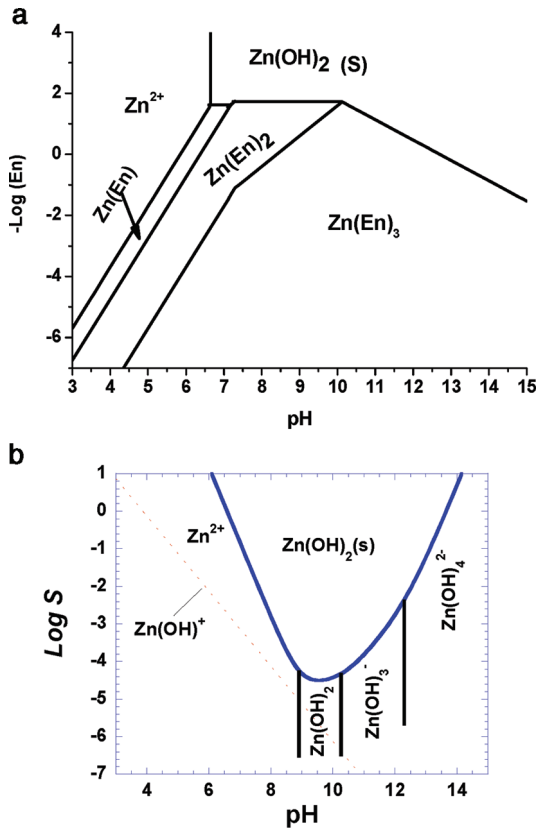

Figure 1. (a) Pourbaix-like diagram of Zn−En complexes for $[Zn^{2+}] = 0.72$ Mol/L. The equilibrium constants reported by Ringbom[21] were used. (b) Phase stability diagram for the $Zn(OH)_2-H_2O$ system at 25 °C as a function of the pH. The dashed line denotes the thermodynamic equilibrium between Zn^{2+} and $Zn(OH)^+$ ions. The boundaries were calculated on the basis of the equilibria and thermodynamic data reported by Martell et al.[31]

Photoluminescence (PL) measurements of the ZnO and Zn/ZnO nanorod samples were performed at room temperature using an excimer pulsed laser (Lambda Physics, COMPex102) emitting at 248 nm and 30 ns pulse duration as excitation source. The UV-light was sent to a SiO_2 wafer containing the ZnO or ZnO-capped Zn nanorods. The laser fluence was varied in the range of 15−8 mJ/cm^2. The resulting luminescence was filtered by a glass slide in order to block the laser emission line. The emitted light was then collected perpendicular to the laser direction by a quartz optical fiber light guide and sent to a 50 cm focal length spectrometer (Acton Research, Spectra Pro 500i) fitted with a 150 lines/mm grating. The dispersed beam was analyzed by an ICCD 1024 × 1024 camera (PI-MAX:1024 UV from Princeton Instruments). The integration time was varied from 5 to 50 ns and the signal was stored in a PC. The ICCD camera was synchronized with the pulsed laser using a Stanford delay generator model DG-535.

The fluorescence spectra of the Zn−En solutions, previously autoclaved at 92 °C, were measured using a Perkin-Elmer Precisely LS55 fluorescence spectrometer.

Results and Discussion

Ethylendiamine is a bidentate ligand which reacts with the zinc ions to give the $[Zn(En)_N]^{(Z-N)+}$ complexes in aqueous solutions. The equilibrium distribution showed by the different Zn complexes is schematically depicted by the Pourbaix-like diagram in Figure 1a. The figure shows the phase stability for the $Zn(OH)_2$−ZnEn complexes at 25 °C. The boundaries were calculated on the basis of the equilibria and the thermodynamic data reported by Ringbom.[9] The depicted lines represent the total concentration of the soluble species as a function of the ligand concentration and pH, i.e., the solubility of the zinc

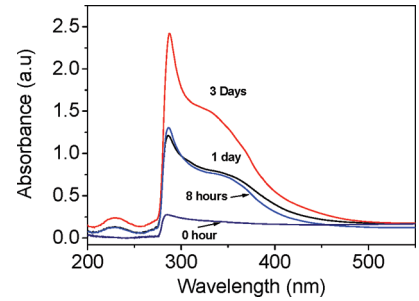

Figure 2. Optical absorption spectra of Zn−En solutions annealed at 92 °C for different times. The sharp peak appearing at 280 nm is associated with the absorption edge of the solvent.

hydroxide phase. Using the diagram, we can predict the formation of homogeneous Zn−En precursors by a careful selection of the En concentration and controlling the pH of the solution. In this work, buffer solutions were not employed to control the pH of the Zn−En precursor solutions. As described above, the basic pH value that was originally imposed by the En ligand was decreased with the addition of the Zn^{2+} cations. A similar pH decrease effect was also observed with other metal−En complexes such as Pt−En or Pd−En (not discussed here). This effect was first studied by Block and Balair in the 1950s.[10−12] As the first step of the reaction, the metallic cations get complexed by the En ligand, forming the $[M(En)_2]^{Z+}$ species. These complexes then participate in a subsequent acid−base equilibrium to give the deprotonated $[M(En)(En-H)]^{(Z-1)+}$ species as follows

$$[M(En)_2]^{Z+} + En \leftrightarrow [M(En)(NH_2-CH_2-CH_2-NH)]^{(Z-1)+} + En-H^+ \quad (1)$$

where $En = NH_2-CH_2-CH_2-NH_2$. The formation of a Block (Balair)-like deprotonated species such as $[Zn(En)(En-H)]^+$ or $[Zn(En)_2(En-H)]^-$, etc., can explain the observed pH decrease by the loss of a proton from the ethylendiamine ligand. Also, from Figure 1, it can be noted that if we are working with pH values less than 10.11, then the predominant equilibrium is

$$Zn(OH)_2(s) + 3HEn^+ = ZnEn_3^- + H^+ + 2H_2O \quad (2)$$

where the pH decrease promotes the dissolution of the solid phase and thus the formation of the more stable $ZnEn_n$ species.

As mentioned earlier, on thermal treatment at 92 °C we also observed a color change of the solution which goes from transparent to pale yellow. This change was also monitored by measuring the UV−vis absorption spectra of Zn−En precursor solutions. As shown in Figure 2, after few hours of thermal treatment, the absorption spectra of Zn−En solutions present two absorption bands with maxima at around 230 nm (5.3 eV) and 345 nm (3.5 eV). These bands have two different origins. In the few works that deal with zinc nanoparticles implanted in SiO_2 matrix, the observed absorption band centered at about 5.1 eV was associated with the zinc surface plasmon resonance (SPR).[13,14] However, very recently, Zeng et al. observed an SPR peak at 242 nm (5.12 eV) for solutions containing ZnO/Zn nanoparticles in water, prepared by laser ablation.[15] From Figure 2, it is not only observed that the 5.3 eV absorption band remained after the formation of zinc nanorods, but also its intensity increased a bit with the thermal treatment time, which suggests the presence of colloidal Zn particles in the autoclaved Zn−En solutions studied here.

It is well-known that the occurrence of ZnO colloidal particles is possible even in the absence of organic ligands and/or

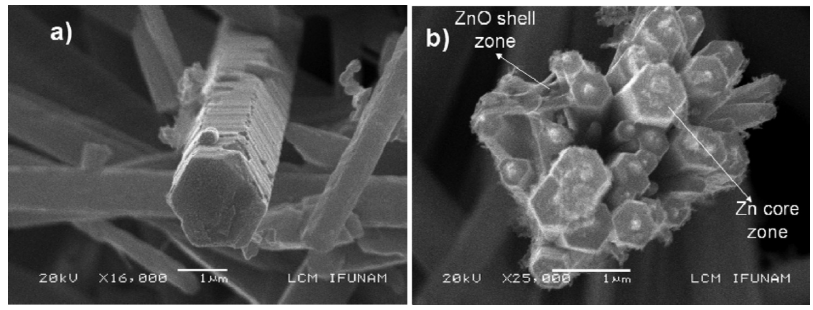

Figure 3. SEM micrograph of (a) Zn metallic nanorods exhibiting full-grown hexagonal habit, (b) ZnO-coated Zn metallic rods after thermal treatment at 92 °C.

surfactants.[16] For diluted solutions, e.g., solutions with a $[Zn^{2+}] \approx 1 \times 10^{-4}$ M, controlling the pH between 9 and 11 promotes the formation of hydroxyl complexes such as $Zn(OH)_2(aq)$ and $Zn(OH)_4^{2-}$ (see Figure 1). Under these conditions, the equilibrium of the eq 3 moves to the right as the chemical potential of the OH^- species increases with the increase of the pH

$$OH^- + OH^- \leftrightarrow O^{2-} + H_2O \quad (3)$$

once these hydroxyl complexes transform into the solid phases, the Zn−O−Zn bonds are then formed because of the dehydration process as follows

$$Zn(OH)_n^{2-n} + Zn(OH)_n^{2-n} \leftrightarrow Zn_2O(OH)_{2n-2}^{4-2n} + H_2O \quad (4)$$

where $n = 2$ or 4.[17] Thus the crystal structure of colloidal ZnO particles is gradually constructed by dehydration between OH^- species on the surface of the growing crystals and the OH^- groups in the solution. As a result, colloidal ZnO suspensions are easily obtained from the ligand-free Zn(II) solutions for a pH range 9−11.[16,18] Moreover, the evolution of colloidal ZnO particles to hexagonal ZnO rods is observed by increasing the pH of the Zn(II) precursor solutions with complexing bases as ammonia and ammonia salts as described in ref 17.

Our SEM and TEM analysis revealed the presence of ZnO nanoparticles anchored at the Zn/ZnO rods surface (Figures 3a and 5). The SEM micrograph of Figure 3a reveals the presence of straight Zn metallic nanorods with clear hexagonal habit. From Figure 3b, it is possible to observe the formation of Zn/ZnO core−shell structures and other structures that are coated with ZnO nanoparticles.

The formation of Zn/ZnO core−shell nanostructures is even clear from the HRTEM images of the samples. The core region of the linear structures is formed by metallic Zn, and the shell corresponds to a layer of wurtzite phase ZnO growing epitaxially over Zn rod (Figure 4b). In the Figure 4b, it is possible to observe a Zn rod grown along the [0002] direction at the core region, and the epitaxial relationship between the Zn/ZnO is $[0002]_{Zn}/[0100]_{ZnO}$. Such epitaxial growth of ZnO over Zn was also reported by other synthesis approach.[19] The other lattice plane observed in the micrograph 4b for ZnO shell corresponds to (0101) for which the *d*-space matches to 0.247 nm for the ZnO counterpart with the lattice fringes shown by the metallic Zn core wire. This analysis can be clarified studying the FFT in the Zn core zone and the corresponding FFT in the ZnO shell zone (see the Supporting Information). In Figure 4c, the EDS spectrum of the core region corresponds to Zn without oxygen, whereas the EDS spectrum of the peripheral region corresponds to ZnO shell (Figure 4d). The EDS analysis in TEM was performed with a 1 nm spot size of the electron beam.

In Figure 5, the nature of these particles is disclosed. Figure 5a shows a solid Zn metallic nanorod with nanoparticles attached to it. The corresponding EDS analysis of the nanorod shows the absence of oxygen peak (Figure 5b). Meanwhile, the EDS analysis obtained at the peripheral nanoparticles shows the presence oxygen peak (Figure 5d). The high-resolution TEM micrograph presented in Figure 5c confirms the presence of ZnO nanoparticles of around 5 nm size oriented along several zone axes over the core Zn nanorod. These results lead us to believe that some of suspended Zn nanoparticles were deposited onto the zinc rod surface and subsequently oxidized to ZnO nanoparticles on thermal treatment at 240 °C.

The 345 nm absorption band in Figure 2 can be attributed to the exciton absorption of ZnO particles, although its position is quite different from those reported for ZnO nanoparticles of radius higher than its Bohr radius (1.8 nm).[17,18] A very similar depression of the ZnO exciton value and PL emission features were also observed in ZnO/Zn colloidal suspensions that were stabilized with sodium dodecyl sulfate.[15,17] We believe the depression of the exciton peak could be associated with a coordination effect of the used ethyliendiamine ligand with the crystalline planes of ZnO nanostructures.

A blue-green PL emission centered at around 442 nm in the PL spectrum of the Zn−En solution treated for 3 days at 92 °C (Figure 6) confirms the presence of ZnO particles suspended in the Zn-En solutions. From our results, it is clear that the strong interactions between the En ligands, the H^+ species, and the colloidal ZnO/Zn particles might be directly involved with the observed growth behavior and optical properties of the nanostructures.

Generally, for solid−liquid interfaces, the local equilibrium concentration of the species which compose the liquid phase depends on the local curvature of the solid phase. A variation of the solid curvature promotes an equilibrium change, causing the transport of species from high-concentration regions (high curvature) to low-concentration regions (low curvature). These capillary forces provide the driving force for the growth of larger solid particles at the expense of smaller ones. Such coarsening effects due to capillary forces at solid phase boundaries are generally termed the Ostwald ripening process.[20,21] The study of the ripening process for the Zn−En system is out of the scope of this work. However, a very simple mechanism that could help us to understand the ZnO rod formation can be deduced from the experiments and the Block (Balair)-like equilibriums. As shown in Figure 1a, for the pH range 9−10.11, the hydroxide dissolution is controlled by the ZnEn complex formation at 25 °C

$$Zn(OH)_2(s) + n\mathrm{En} + 2H^+ = Zn(\mathrm{En})_n + 2H_2O \quad (5)$$

It should be noted that this is the pH range imposed by the saturation of the En solution with the zinc salt ($C = 0.72$ M). At this temperature, the $Zn(OH)_2$ precipitation can not be

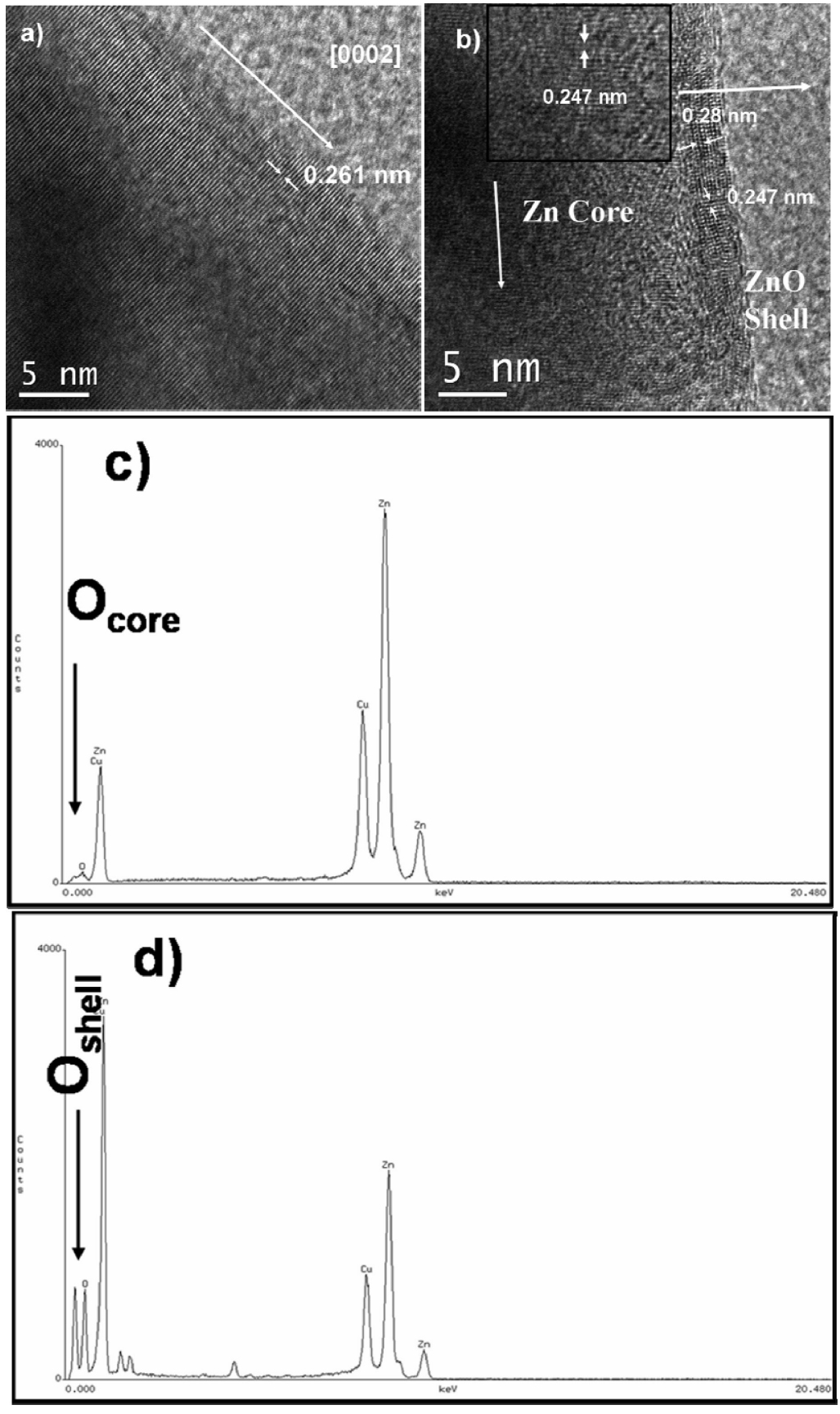

Figure 4. (a) Typical HRTEM micrograph of ZnO nanorods growing along [0002] direction; (b) HRTEM micrograph of a coaxial Zn/ZnO nanorod. The core corresponds to a metallic Zn nanorod in the wurtzite phase grown along the [0002] direction (*d*-space shown in the inset, 0.247 nm), whereas the shell corresponds to a wurtzite ZnO layer growing epitaxially along the [0100] direction perpendicularly to the [0002] direction of the Zn core wire. The other reflection observed in the micrograph for the ZnO shell corresponds to [0101], for which the *d*-space matches to 0.247 nm for the ZnO counterpart with the lattice fringes shown by the metallic Zn core wire. (c) EDS spectrum of the core region corresponds to Zn without oxygen; (d) EDS spectrum of the peripheral region corresponds to ZnO shell. The EDS analysis in TEM was performed with a 1 nm spot size of the electron beam.

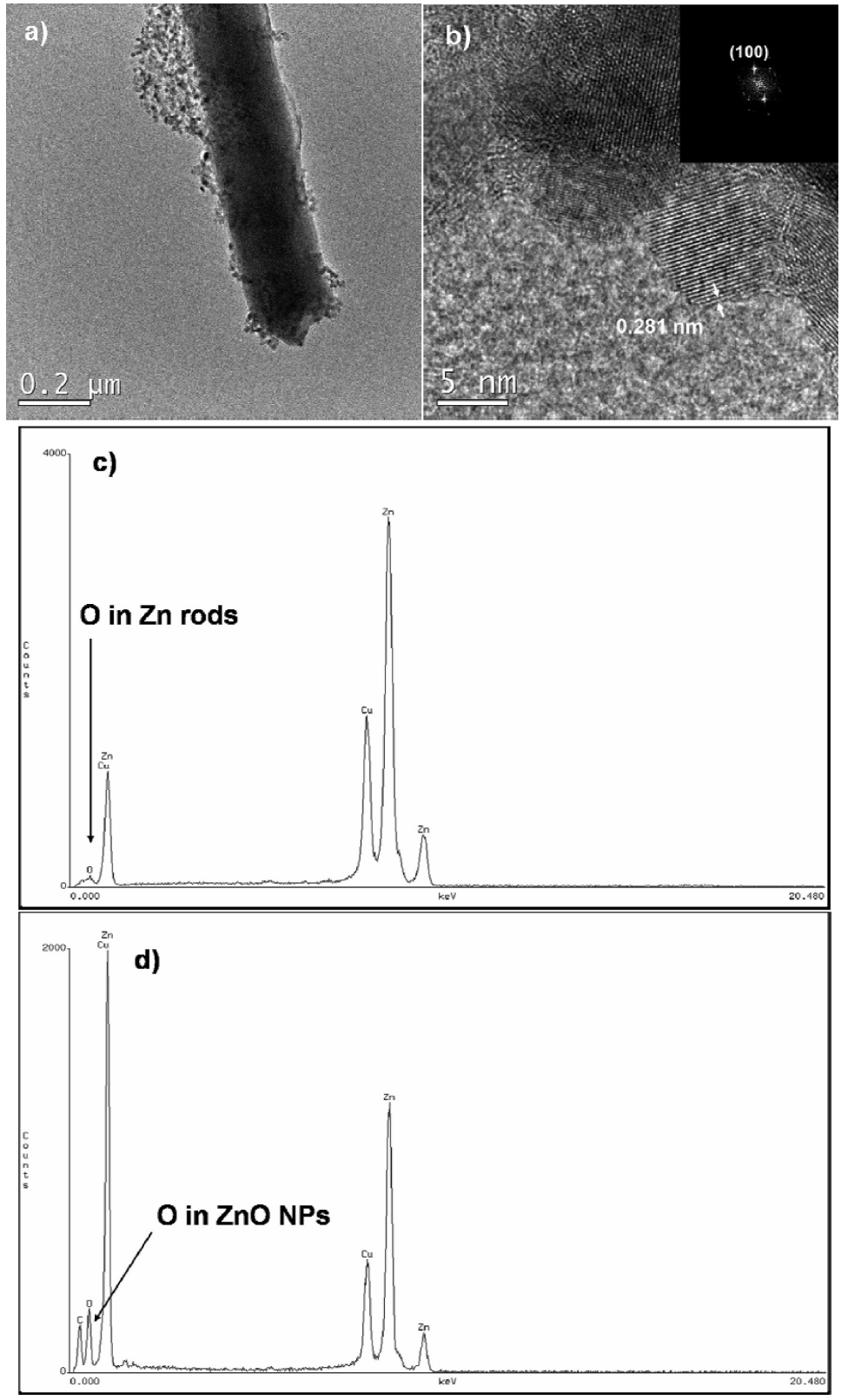

Figure 5. (a) Low-magnification TEM micrograph of a solid metallic Zn rod coated with ZnO nanoparticles; (b) HRTEM of the ZnO nanoparticles over the metallic Zn core; the particles are oriented at several zone axis with respect to the electron beam; (c) EDS spectrum of the metallic Zn core showing the absence of oxygen; (d) EDS analysis from the superficial ZnO nanoparticles.

observed even by increasing the pH from 9 to 10.11 with the addition of some drops of saturated NaOH solution (see Figure 1a). Moreover, the formation of solid $Zn(OH)_2$ is not yet observed for pH values that are slightly higher than 10.11 but less than 11.3. Because of the tampon effect imposed by the ethylendiamine ligands, the increase in pH value higher than 11.3 can not be observed with the addition of more NaOH solution. However, as can be followed from the Figure 1a, at pH values higher than 10.11, the ZnEn complex becomes thermodynamically unstable. Under hydrothermal conditions (92

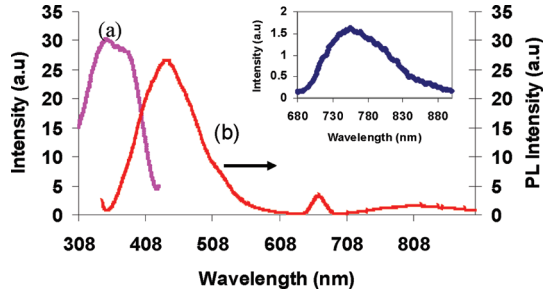

Figure 6. Room-temperature (a) excitation and (b) emission spectra of a Zn−En solution ($[Zn^{2+}]$ = 0.72 mol/L) after hydrothermal treatment at 92 °C for 3 days. The excitation spectrum was recorded for an emission band at about 808 nm. The emission spectrum was obtained using an excitation line at 335 nm. The peak at about 670 nm is the second harmonic of the excitation line. The inset shows the emission spectrum of a 10% v/v En solution, measured using the same excitation line at 335 nm.

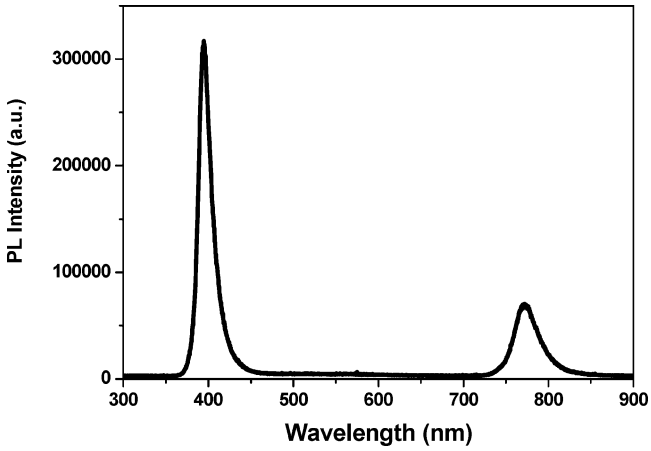

Figure 7. Typical room-temperature PL spectrum of Zn−ZnO nanorods obtained by exciting with 248 nm laser pulses of 8 mJ/cm^2 intensity.

°C), the ZnO rods were formed instead of the Zn/ZnO core−shell structures when the pH of the autoclaved solution was previously increased to the values higher than 10.11 (Figure 5a). The ZnO rods are formed because of the increase in instability of the ZnEn complexes caused by the temperature increase from 25 to 92 °C. Weakening of the Zn−En bonds induced by the hydrothermal conditions could move the equilibrium of the eq 5 to the left, promoting the ZnO solid formation. As the solid phase must be in intrinsic equilibrium with its soluble counterpart (e.g., $Zn(OH)_2$). a similar dehydration process such as that depicted in eq 4 could be observed and thus a crystal growing process would be carried on by a dehydration process.

On the other hand, if ZnEn precursor solutions in which no NaOH was added are now autoclaved, the formation of Zn rods can be observed (Figure 3a). Compared with the ZnO rods, the formation mechanism of the Zn/ZnO core−shell structures is not as simple as it seemed to be. That is, whereas the wurzite ZnO formation does not imply a change in the redox chemistry of the Zn(II) (see eqs 4 and 5) the crystal formation of the Zn core implies a redox change from Zn(II) to Zn(0). On hydrothermal treatments at 92 °C, we observed neither Zn core structures nor ZnO rod formation for ZnEn solutions whose pH was diminished from 9 to about 7 with the addition of some drops of hydrochloric acid. At this pH range, in spite of temperature increase, formation of Zn/ZnO core−shell structures is inhibited because of the formation of the complexes (Figure 1a)

$$[Zn(En)_2NH_2CH_2CH_2NH_2] + En \leftrightarrow [Zn(En)_2(En-H)]^{2-} + En-H^+ \quad (6)$$

$$[Zn(En)NH_2CH_2CH_2NH_2] + En \leftrightarrow [Zn(En)(En-H)]^- + En-H^+ \quad (7)$$

Such a decrease in pH value would provide additional degree of stability to the ZnEn complexes (see eq 5). We observed the formation of Zn/ZnO core−shell rods by autoclaving ZnEn solutions with pH values between 9 and 10.11. As mentioned earlier, these pH values of the solution were imposed by the addition of the zinc salt to the En solution. However, the formation of these core−shell rod structures must be influenced by some additional parameters, like the degree of saturation of zinc ions and concentration of ethylendiamine, a part from the temperature and the pH of the reaction solution, which need further careful studies.

The room-temperature photoluminescence (PL) spectrum of a core−shell Zn/ZnO sample annealed at 240 °C in air is shown in Figure 7. An emission band peaking at about 394 nm (3.14 eV) was observed. Several UV emissions in the 3.27−3.3 eV range have been reported for ZnO nanostructures[22] and thin films[23] and assigned as near band edge or free exciton emissions. Srikant and Clarke[24] have reported both the 3.3 and 3.15 eV emissions for their bulk ZnO samples. They associated the 3.15 eV emission with deep donor/acceptor levels. In fact, deep-level transient spectroscopy (DLTS) measurements on bulk ZnO varistors revealed the existence of an intrinsic donor level at ~0.15−0.17 eV below the conduction band.[25] We believe that the 3.14 eV emission in our Zn/ZnO core−shell structures arises from donorlike point defects.

The optoelectronic quality of ZnO nanostructures is frequently measured by the intensity ratio between the NBE (near-band-edge) and the deep-level emissions.[26] In our case, the TEM observations revealed the ZnO shell structures around zinc core are mostly in single crystalline phase. However, as they frequently grow perpendicular to the [0002] (d_{0002} = 0.606 nm) direction of the 1D Zn cores, there must have many structural defects such as dislocations and stacking faults at the interfaces.

As is shown in the Figure 6, the Zn−En solutions presents an IR emission centered at above 808 nm. Such emission overlaps with another band at about 750 nm arising from ethylenediamine emission (inset of Figure 6), which was obtained using the same excitation line (335 nm). However, by measuring the excitation spectra of the 808 nm emission line, we obtained the 375 nm peak that is associated with the ZnO band edge (Figure 8). Our results are in accordance with results reported by Lauer, who demonstrated that the excitation spectra of IR emission in ZnO bulk crystals is made of three bands centered at above 3.3, 3.1, and 2.94 eV, respectively.[27] Therefore, the IR emission observed in the Zn−En solutions suggests the presence of ZnO colloidal particles in the autoclaved solutions. The nature of the IR emission band in ZnO remains unresolved. The IR emission at about 1.7 eV was reported for ZnO bulk crystals and powders after air annealing at temperatures between 900−1000 °C.[27] However, the 1.7 eV emission always appeared as the tail end of another emission centered at about 2.2 eV. The 2.2 eV emission is assumed to be originated from the donor centers slightly below the conduction band. On the other hand, the 1.7 eV emission, occasionally called as red emission in ZnO, can be associated

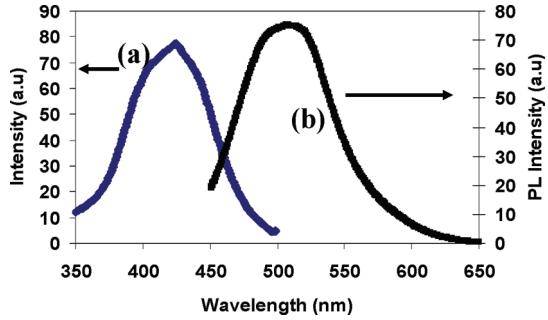

Figure 8. The (a) excitation and (b) emission spectra of a Zn−En solution ($[Zn^{2+}] = 0.72$ mol/L) after hydrothermal treatment at 92 °C for 1 week. The measurement conditions were the same as those in Figure 6.

with a transition from a state at the edge of the conduction band to a hole trapped in a localized state, which could be introduced by alkali impurities (e.g., Li, Na, or other metal alkali impurities).[28]

Unlike the emissions observed for the Zn−ZnO rods structures, the PL emission spectra of Zn−En solutions presented a broad blue-green emission centered at above 442 nm (Figures 6). Similar PL features were observed for Zn−En solutions whose time of thermal treatment was less than 3 days. However, as is shown in Figure 8, the excitation and emission spectra change drastically for the Zn−En solutions that were autoclaved for several days. For these solutions, an evolution of the emission from the blue-green to green is appreciated. Generally, in ZnO, the deep level emission consists of a green emission at around 520 nm and a near-yellow emission around 640 nm.[29] Such a change in the PL emission of the Zn−En solutions indicates an increase in the strain and deep level defects of the ZnO colloidal particles. This is supported by the photon energy associated with the excitation spectra of the Figure 8 which equals to ∼2.94 eV and is attributed to the direct excitation of substitutional luminescence centers in the ZnO.[27,30] The obtained results not only demonstrate the interesting PL properties of the Zn/ZnO core−shell nanorod structures but also for the Zn−En precursor solutions at different stages of autoclaving.

Conclusions

One-dimensional Zn/ZnO core−shell nanostructures were obtained by a low-temperature solvothermal approach. The ZnO shells grow over crystalline Zn metallic nanorods following the $[0002]_{Zn}/[0100]_{ZnO}$ epitaxial relation. The epitaxial ZnO layers might have several structural defects at the interface due to lattice mismatch with metallic zinc. The presence of polycrystalline ZnO nanoparticles over some of the crystalline Zn rods suggests that the epitaxial ZnO layers form through the coalescence of small ZnO particles, formed at the initial stage of the oxidation of Zn nanoparticles in the reaction mixture.

Formation of pure metallic Zn, ZnO, and Zn/ZnO core−shell nanostructures through ethylenediamine mediated hydrothermal synthesis depends strongly on the reaction conditions like pH of the reaction solution, temperature of autoclaving, along with the concentration of zinc ions. Therefore, using this low-temperature process, one can synthesize either of these nanostructures just be adjusting the reaction conditions. The process can be applied for producing other hybrid nanostructures.

Acknowledgment. This work was financially supported by CONACyT-Mexico (Grant number 52715, 47272), CUDI and DGPA-UNAM system by postdoctoral fellowship, and IN119608-3, IN110109-3 grants. The authors thank to Roberto Hernandez for his support in the SEM characterization. The authors thank the Central Microscopy facilities of the Institute of Physics, UNAM, for providing the microscope tools used in this work. Photoluminescence measurements were made at the Photophysics Lab at UNAM.

Supporting Information Available: Fast Fourier transfrom from HRTEM images (PDF). This material is available free of charge via the Internet at http://pubs.acs.org.

References

(1) Nicoll, F. H. *Appl. Phys. Lett.* **1966**, *9*, 13.
(2) Hvam, J. M. *Solid State Commun.* **1973**, *12*, 95.
(3) Klingshirn, C. *Phys. Status Solidi B* **1975**, *71*, 547.
(4) Bagnall, D. M.; Chen, Y. F.; Zhu, Z.; Yao, T.; Koyama, S.; Shen, M. Y.; Goto, T. *Appl. Phys. Lett.* **1997**, *70*, 2230.
(5) Wang, Z. L. *J. Phys: Condens. Matter* **2004**, *16*, R829.
(6) Service, R. F. *Science* **1997**, *276*, 356.
(7) Newton, M. C.; Warburton, P. A. *Mater. Today* **2007**, *10*, 50.
(8) Pal, U.; Santiago, P. *J. Phys. Chem. B* **2005**, *109*, 15317.
(9) Ringbom. A. *Complexation in Analytical Chemistry*; John Wiley & Sons: New York, 1963; p 352.
(10) Block, B. P.; Bailar, J. C., Jr. *J. Am. Chem. Soc.* **1951**, *73*, 4722.
(11) Watt, G. W.; Layton, R. *J. Am. Chem. Soc.* **1960**, *82*, 4465.
(12) Watt, G. W.; McCarley, R. C. *J. Am. Chem. Soc.* **1957**, *79*, 3315.
(13) Cheng, J.; Mu, R.; Ueda, A.; Wu, M. H.; Tung, Y.-S.; Gu, Z.; Henderson, D. O.; White, C. W.; Budai, J. D.; Zuhr, R. A. *J. Vac. Sci. Technol., A* **1998**, *16*, 1409.
(14) Lee, J. K.; Tewell, C. R.; Schulze, R. K.; Nastasi, M.; Hamby, D. W.; Lucca, D. A.; Jung, H. S.; Hong, K. S. *Appl. Phys. Lett.* **2005**, *86*, 183111.
(15) Zeng, H.; Cai, W.; Li, Y.; Hu, J.; Liu, P. *J. Phys. Chem. B* **2005**, *109*, 18260.
(16) Wong, E. M.; Bonevich, J. E.; Searson, P. C. *J. Phys. Chem. B* **1998**, *102*, 7770.
(17) Yamabi, S.; Imai, H. *J. Mater. Chem.* **2002**, *12*, 3773.
(18) Wong, E. M.; Searson, P. C. *Appl. Phys. Lett.* **1999**, *74*, 2939.
(19) Hu, J. Q.; Li, Q.; Meng, X. M.; Lee, C. S.; Lee, S. T. *Chem. Mater.* **2003**, *15*, 305.
(20) Usui, H.; Shimizu, Y.; Sasaki, T.; Koshizaki, N. *J. Phys. Chem. B* **2005**, *109*, 120.
(21) Lifshitz, I. M.; Slyozov, V. V. *J. Phys. Chem. Solids* **1961**, *19*, 35.
(22) Kong, Y. C.; Yu, D. P.; Zhang, B.; Fang, W.; Feng, S. Q. *Appl. Phys. Lett.* **2001**, *78*, 407.
(23) Tang, Z. K.; Wong, G. K. L.; Kawasaki, M.; Ohtomo, A.; Koiinuma, H.; Segawa, Y. *Appl. Phys. Lett.* **1998**, *72*, 3270.
(24) Srikant, V.; Clarke, D. R. *J. Appl. Phys.* **1998**, *83*, 5447.
(25) Greuter, F.; Blatter, G. *Semiconduct. Sci. Technol.* **1990**, *5*, 111.
(26) Bagnall, D. M.; Chen, Y. F.; Shen, M. Y.; Zhu, Z.; Goto, T.; Yao, T. *J. Cryst. Growth* **1998**, *184/185*, 605.
(27) Lauer, R. B. *J. Phys. Chem. Solids* **1973**, *34*, 249.
(28) Ortiz, A.; Falcony, C.; Hernández JGarcía, A. M.; Alonso, J. C. *Thin Solid Films* **1997**, *293*, 103.
(29) Ong, H. C.; Du, G. T. *J. Cryst. Growth* **2004**, *265*, 471.
(30) Vanheusden, K.; Seager, C. H.; Warren, W. L.; Tallant, D. R.; Voigt, J. A. *Appl. Phys. Lett.* **1996**, *68*, 403.
(31) Martell, A. E. Hancock, R. D. *Metal Complexes in Aqueous Solutions*; Plenum Press: New York, 1996.

CG8001493